Determination of a stress-dependent rock-physics model using anisotropic time-lapse tomographic inversion

Nicolas Mastio, Pierre Thore, Marianne Conin, Guillaume Caumon

GEOPHYSICS, VOL. 85, NO. 4 (JULY-AUGUST 2020); P. C141–C152, 13 FIGS.
10.1190/GEO2019-0526.1

Determination of a stress-dependent rock-physics model using anisotropic time-lapse tomographic inversion

Nicolas Mastio[1], Pierre Thore[2], Marianne Conin[3], and Guillaume Caumon[3]

ABSTRACT

In the petroleum industry, time-lapse (4D) studies are commonly used for reservoir monitoring, but they are also useful to perform risk assessment for potential overburden deformations (e.g., well shearing, cap-rock integrity). Although complex anisotropic velocity changes are predicted in the overburden by geomechanical studies, conventional time-lapse inversion workflows only deal with vertical velocity changes. To retrieve the geomechanically induced anisotropy, we have adopted a reflection traveltime tomography method coupled with a time-shift estimation algorithm of prestack data of the baseline and monitor simultaneously. For the 2D approach, we parameterize the anisotropy using five coefficients, enough to cover any type of anisotropy. Before applying the workflow to a real data set, we first study a synthetic data set based on the real data set and include velocity variations between baseline and monitor found in the literature (vertical P-wave velocity decrease in the cap rock and isotropic P-wave velocity change in the reservoir). On the synthetics, we measure the angular ray coverage necessary to retrieve the target anisotropy and observe that the retrieved anisotropies depend on the offset range. Based on a synthetic experiment, we believe that the acquisition of the real case study is suitable for performing tomographic inversion. The anisotropic velocity changes obtained on three inlines separated by 375 m are consistent and show a strong positive anomaly in the cap rock along the 45° direction (the δ parameter in Thomsen notation), whereas the vertical velocity change is surprisingly almost negligible. We adopt a rock-physics explanation compatible with these observations and geologic considerations: a reactivation of water-filled subvertical cracks.

INTRODUCTION

The repetition of seismic surveys during hydrocarbon reservoir production is a widely used monitoring method. However, the interpretation of the shifts between vintages of time-lapse seismic data in terms of fluid, mechanical and geometric changes is challenging (Røste et al., 2006) especially with respect to the time-lapse effect in the overburden. Indeed, overburden time shifts have been observed in a wide range of time-lapse studies: chalk fields, e.g., Valhall (Barkved and Kristiansen, 2005; Hatchell et al., 2005); high-pressure, high-temperature fields, e.g., Elgin, Franklin and Kristin (De Gennaro et al., 2008; Dybvik et al., 2009); sandstone reservoirs at normal pressure and temperature, e.g., Snorre field (Røste et al., 2015); and turbidite sands fields, e.g., the Genesis and Dalia fields (Rickett et al., 2007; Rodriguez-Herrera et al., 2015). Except in rare cases in which subsidence is significant (e.g., Ekofisk field — Guilbot and Smith, 2002), shifts in the time-lapse vintages are predominantly due to the accumulation of small velocity changes.

These velocity changes are the signature of the geomechanical response to the reservoir compaction. Because linear elasticity is incompatible with velocity change, nonlinearity has to be considered. For instance, Prioul et al. (2004) propose using the "third-order" elasticity coefficients theorized by Hearmon (1953) to express the stress dependence of elastic properties. Laboratory experiments on different shales have been performed to calibrate these coefficients. Based on geomechanical models and published third-order elasticity coefficients, Fuck et al. (2009) and Herwanger and Horne (2009) show that the reservoir production creates anisotropic velocity changes within the reservoir and the surrounding rocks.

Manuscript received by the Editor 14 August 2019; revised manuscript received 13 March 2020; published ahead of production 10 June 2020; published online 10 June 2020.
[1]Université de Lorraine, CNRS, CREGU, GeoRessources, UMR 7359, Nancy 54000, France; Total S.A., CSTJF, Avenue Larribau, Pau cedex 64018, France. E-mail: nicolas.mastio@club.fr (corresponding author).
[2]Total S.A., CSTJF, Avenue Larribau, Pau cedex 64018, France. E-mail: pierre.thore@total.com.
[3]Université de Lorraine, CNRS, CREGU, GeoRessources, UMR 7359, Nancy 54000, France. E-mail: marianne.conin@univ-lorraine.fr; guillaume.caumon@univ-lorraine.fr.

Despite numerous theoretical evidences of anisotropy, the overburden time-lapse velocity change is usually considered vertical for operational purposes. One-dimensional time-lapse inversion is common in practice (Williamson et al., 2007). Furthermore, the rock physics that can relate the velocity change to the stress change is unknown. This missing rock-physics model is substituted by the empirical model of Hatchell and Bourne (2005) and Røste et al. (2006), which assumes a linear relationship between the velocity change and the relative thickness variations of the overburden layers.

To overcome the limitations of a trace-by-trace inversion, Edgar and Mastio (2017) propose a prestack tomographic inversion method that considers an isotropic time-lapse velocity change. The authors build a ray-based inversion, which accounts for velocity changes along different rays. It consists in coupling a trace-alignment procedure with the linearized reflection traveltime tomography to construct a nonlinear scheme, which looks for a smooth time-lapse velocity change that aligns the vintages of time-lapse prestack seismic data. This method avoids the 1D approximation and retrieves velocity changes globally while respecting the ray theory.

In the present contribution, the tomographic-inversion method is adapted to tackle an anisotropic perturbation in an initial model assumed isotropic (Červený, 2001). Finding a proper parameterization with respect to the data and the aperture width is essential when using an anisotropic model to fit seismic data (Alkhalifah and Plessix, 2014; Oh and Alkhalifah, 2016). The problem is very ill posed. Prieux et al. (2011) apply full-waveform inversion and show that a nearly equivalent match of the data can be obtained with either an isotropic or an anisotropic velocity model. The parameterization and the initial model must be carefully chosen to obtain a meaningful result.

In the literature, the velocity change in the overburden is assumed to be mainly vertical. In this paper, we include in a synthetic example a vertical velocity decrease in the overburden and an isotropic velocity increase in the reservoir. We show that our method can retrieve the anisotropic perturbation induced in the velocity model when the acquisition range is large enough. We apply the method to a vintage time-lapse data set of a gas field with an unknown anisotropy perturbation. Our method shows a surprising 45° and horizontal velocity decrease in the cap rock. A plausible rock-physics model based on the homogenization of cracks compatible with the anisotropy of the velocity change and the stress change is derived.

METHODS

Time shifts induced by an anisotropic velocity change

The velocity change between the base and the monitor has the effect of shifting the reflector locations. Measuring these time-lapse shifts allows us to do a tomographic reconstruction of the velocity change. However, in the case of an anisotropic velocity change, all of the elastic parameters cannot be retrieved because only the longitudinal waves are considered.

Traveltime perturbation

The traveltime perturbation expression has been established in numerous ways. For an isotropic smooth medium, based on Fermat's principle in isotropic media (Nolet, 1987; Aki and Richards, 2002), the traveltime perturbation Δt along a ray Ω_0 is linearized as

$$\Delta t = -\int_{\Omega_0} \frac{\Delta v}{v_0} dt, \tag{1}$$

where $\Delta v/v_0$ is the relative velocity change between the referenced and the perturbed model and dt is the time increment of the ray. For a smooth anisotropic medium, based on the Lagrangian approach (Nowack and Pšenčík, 1991) and the Hamiltonian approach (Červený, 2001), the traveltime perturbation becomes (using the Einstein summation rules)

$$\Delta t = -\frac{1}{2}\int_{\Omega_0} \Delta a_{ijkl} p_i p_j g_k g_l dt, \tag{2}$$

where $\mathbf{p}$ is the slowness vector, $\mathbf{g}$ is the polarization vector, and a_{ijkl} is the density-normalized elastic tensor $a_{ijkl} = c_{ijkl}/\rho$ (c_{ijkl} is the fourth-order elastic tensor and ρ is the rock density), which has the same dimension as velocity squared. At a first-order approximation, the traveltime perturbation is suitable for solving the tomographic inverse problem (Chapman and Pratt, 1992; Le Bégat and Farra, 1997).

For simplicity of presentation, we consider longitudinal elastic waves only propagating in an initially isotropic heterogeneous medium at velocity v_0. In this case, the slowness vector $\mathbf{p}$ and polarization vector $\mathbf{g}$ have the same direction as the propagation direction $\mathbf{n}$. This can be written as

$$\mathbf{p} = \frac{1}{v_0}\mathbf{n}, \quad \mathbf{g} = \mathbf{n}, \tag{3}$$

and the infinitesimal anisotropic velocity change as

$$\frac{\Delta v}{v_0} = \frac{\Delta a_{ijkl}}{2{v_0}^2} n_i n_j n_k n_l. \tag{4}$$

Two mediums are considered in the context of time-lapse seismics. The first one is the reference medium being the field before production. The second one consists of a snapshot of the same field after a production period. The seismic imaging of these medium corresponds to the baseline and the monitor. We expect the velocity field of the second medium to be slightly different from that of the reference medium due to the change in the effective stress field in the cap rock and in the reservoir induced by the production of reservoir fluids.

Parameterizations of the longitudinal wave anisotropy

In the case of anisotropy, inverse problems applied to seismic data suffer from ill-conditioning and nonuniqueness (Alkhalifah, 1997; MacBeth, 2002; Oh and Alkhalifah, 2016; Kazei and Alkhalifah, 2018b; Podgornova et al., 2018) because of the large number of parameters needed to describe the material behavior in the general case and the limited offset acquisition.

Equation 4 shows that the ray traveltime depends on the density-normalized elastic parameters Δa_{ijkl}. Nevertheless, all of the 21 independent elastic parameters cannot be retrieved for two main reasons. The first one is that the reference interval velocity model influences the angle coverage for a given acquisition length, limiting the range of illumination angles available to characterize the

elastic coefficients. The second reason is that the longitudinal traveltime perturbation is influenced by 15 parameters only, where the six constants or combinations (c_{11}, c_{22}, c_{33}, $c_{12}+2c_{66}$, $c_{23}+2c_{44}$, and $c_{13}+2c_{55}$) are the most sensitive parameters, with the remaining ones (c_{16}, c_{15}, c_{26}, c_{24}, c_{35}, c_{34}, $c_{14}+2c_{56}$, $c_{25}+2c_{46}$, and $c_{36}+2c_{45}$) having a much smaller influence (Backus, 1970; Every and Sachse, 1992; Kazei and Alkhalifah, 2018a). These 15 parameters correspond to the totally symmetric part of the elastic tensor $s_{ijkl}=(c_{ijkl}+c_{iklj}+c_{iljk})/3$, which can be expressed with the Voigt notation (Love, 1944) as

$$s_{ijkl}=\begin{bmatrix} \boxed{s_{11}} & \boxed{s_{12}} & \boxed{s_{13}} & s_{14} & s_{15} & s_{16} \\ * & \boxed{s_{22}} & \boxed{s_{23}} & s_{24} & s_{25} & s_{26} \\ * & * & \boxed{s_{33}} & s_{34} & s_{35} & s_{36} \\ * & * & * & s_{44} & s_{45} & s_{46} \\ * & * & * & * & s_{55} & s_{56} \\ * & * & * & * & * & s_{66} \end{bmatrix}, \tag{5}$$

where the 15 independent parameters are $s_{11}=c_{11}$, $s_{22}=c_{22}$, $s_{33}=c_{33}$, $s_{15}=c_{15}$, $s_{16}=c_{16}$, $s_{26}=c_{26}$, $s_{24}=c_{24}$, $s_{34}=c_{34}$, $s_{35}=c_{35}$, $s_{12}=(c_{12}+2c_{66})/3$, $s_{13}=(c_{13}+2c_{55})/3$, $s_{14}=(c_{14}+2c_{56})/3$, $s_{23}=(c_{23}+2c_{44})/3$, $s_{25}=(c_{25}+2c_{46})/3$, and $s_{36}=(c_{36}+2c_{45})/3$. The boxed parameters represent the ones most sensitive to the longitudinal wave velocity.

Because the following tomography is performed along inlines, the 2D approach is developed. The anisotropic tomography parameterization problem has already been successfully addressed by Chapman and Pratt (1992) for the case of crosswell tomography, and we decide to use their parameterization with slight modifications. We recall the construction of this parameterization in the following. Considering a system of axes $(O;x_1,x_2,x_3)$ oriented such that x_1 is the horizontal axis, x_2 is the out-of-plane axis, and x_3 is the vertical axis, the polarization vector takes the form $\mathbf{n}=(\sin\theta,0,\cos\theta)$, where θ is the angle between the ray and the vertical axis. In polar coordinates, the anisotropic velocity change in equation 4 can be written as

$$\frac{\Delta v}{v_0}(\theta)=q_1\cos^4\theta+q_2\cos^3\theta\,\sin\theta+2q_3\cos^2\theta\sin^2\theta + q_4\cos\theta\sin^3\theta+q_5\sin^4\theta, \tag{6}$$

where the q_i are functions of the normalized elastic tensor perturbation:

$$q_1=\frac{\Delta a_{33}}{2{v_0}^2},\quad q_2=\frac{\Delta a_{35}}{2{v_0}^2},\quad q_3=\frac{\Delta a_{13}+2\Delta a_{55}}{2{v_0}^2},$$
$$q_4=\frac{\Delta a_{15}}{2{v_0}^2},\quad \text{and}\quad q_5=\frac{\Delta a_{11}}{2{v_0}^2}. \tag{7}$$

The basis functions used in equation 6 are depicted in Figure 1.

This parameterization is general in the sense that it does not assume any material symmetry. The coefficient q_3 in equation 7 is slightly different from the one described in Chapman and Pratt (1992). Using the proposed coefficients, the three parameters q_1, q_3, and q_5 have the same amplitude for an isotropic velocity change enabling the use of the same regularization weights for these parameters in the inverse problem.

In any case, the most sensitive parameters are q_1, q_3, and q_5 (Every and Sachse, 1992). Moreover, q_2 and q_4 are equal to zero if the elastic perturbation has a vertical symmetry direction. In this case, q_1 represents the vertical to subvertical velocity change. It corresponds to the type of parameters that a classic seismogram trace alignment algorithm attempts to retrieve. The term q_3 is the velocity change measured at approximately 45°, and q_5 is the horizontal to subhorizontal velocity change. If the vertical symmetry assumption is not respected, q_2 or q_4 is not equal to zero. In the special case of a weak vertical transverse isotropy elastic perturbation, the velocity change can be written as $\Delta v/v(\theta)=\Delta v/v(0°)+\delta\sin^2\theta\cos^2\theta+\varepsilon\sin^4\theta$ (Thomsen, 1986), which translates to $q_1=\Delta v/v(0°)$, $q_3=\Delta v/v(0°)+\delta/2$ and $q_5=\Delta v/v(0°)+\varepsilon$. In this case, the vertical velocity change q_1 corresponds to the isotropic velocity change, and the differences $2(q_3-q_1)$ and q_5-q_1 measure the anisotropy. For a tilted transversely isotropic material, the three Thomsen parameters, the azimuth, and the dip can be estimated with the five components of $\mathbf{q}$. The transformation is discussed in detail in Chapman and Pratt (1992).

Tomographic inversion

In classic time-lapse inversion, the measured time shifts are exclusively related to a vertical velocity change. However, with vertical information only, the velocity anisotropy cannot be retrieved. The time-lapse velocity change tomography method does not require the vertical assumption. Instead, it models the time shifts applied to each offset as a result of a small velocity perturbation. In our approach, the time-shift estimation is embedded inside the tomographic algorithm.

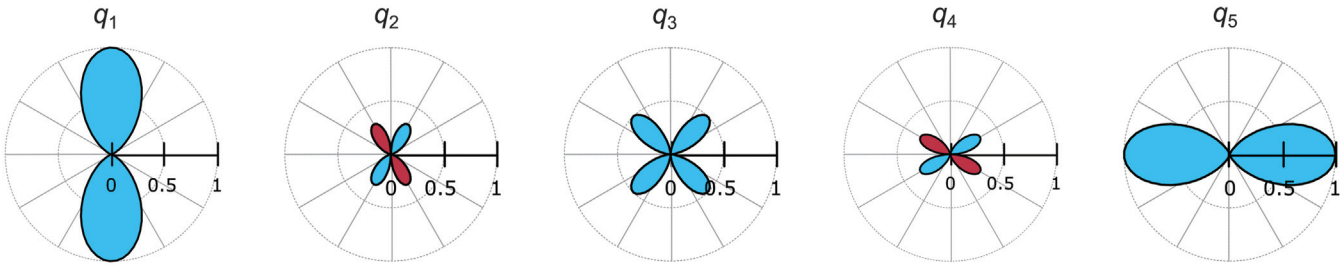

Figure 1. Geometric representation of the basis used in the polar plots. The five functions define general anisotropy in 2D. Each quarter is subdivided into three parts such that each one represents 30°. We can see graphically that q_1 and q_2 are sensitive to polar angles between 0° and 30°, q_3 is sensitive to angles between 30° and 60°, and q_4 and q_5 are sensitive to polar angles between 60° and 90°. Blue indicates positive values, and red indicates negative values.

Time-shifts estimation using arrival-time warping methods

Dynamic time warping (Hale, 2013) and nonlinear least-squares regression (Rickett et al., 2007; Williamson et al., 2007) are examples of alignment algorithms formulated as optimization problems. They attempt to minimize a cost function that depends on a baseline trace $B(t)$ and a monitor trace $M(t)$ having the same source and receiver locations, a depth of interest (in the time domain) τ, and a time shift Δt. For the sake of simplicity, we consider a general expression of the minimization problem, but the following can be adapted to any trace alignment method written as a cost function.

At a given reflection, the measured time shift $\Delta t_{\text{measured}}$ is the solution of the minimization problem:

$$\Delta t_{\text{measured}} = \underset{\Delta t}{\text{argmin}}[r_{\text{TShift}}(\Delta t)]^2, \tag{8}$$

with $r_{\text{TShift}}(\Delta t)$ being the residuals between the baseline trace $B(t)$ and the warped monitor trace $W(M(t), \Delta t)$ within a time window $\Delta\tau$ around the considered reflection; i.e.,

$$r_{\text{TShift}}(\Delta t) = \sum_{t=\tau-\frac{\Delta\tau}{2}}^{\tau+\frac{\Delta\tau}{2}} [B(t) - W(M(t), \Delta t)]. \tag{9}$$

The Jacobian of the trace alignment residual $J_{\text{TShift}}(\Delta t) = \partial r_{\text{TShift}}/\partial \Delta t$ depends only on the monitor trace as

$$J_{\text{TShift}}(\Delta t) = -\sum_{t=\tau-\frac{\Delta\tau}{2}}^{\tau+\frac{\Delta\tau}{2}} \frac{\partial W}{\partial \Delta t}(M(t), \Delta t). \tag{10}$$

In equations 9 and 10, the time window $\Delta\tau$ must be adapted to the considered case because the retrieved time shifts are sensitive to the chosen window length (Mikesell et al., 2015).

The choice of the relevant trace alignment algorithm depends on the time-lapse effect observed on the data set. For instance, if strong amplitude changes occur, including the amplitude term in the trace alignment function can be considered. In the overburden, where very limited amplitude changes are observed, the presented trace alignment algorithm in equations 9 and 10 can be used.

Trace realignment with a smooth anisotropic velocity change

The inverse problem can be written as a minimization problem. We look for the velocity change $\mathbf{q}$ solution of

$$\underset{\mathbf{q}}{\text{argmin}}(\|\mathbf{r}(\mathbf{q})\|^2 + \|\sum_{i=1}^{5} \mu_i \mathbf{L} q_i\|^2), \tag{11}$$

where $\mathbf{r}(\mathbf{q})$ is the residual vector that measures the misalignment between the warped monitor trace window and the baseline and $\mathbf{q}$ is the column vector $(q_1\ q_2\ q_3\ q_4\ q_5)^T$. As with almost all subsurface inverse problems (Gubbins, 2004), a regularization is required to address the problem's ill-posedness and ensure the stability of the tomographic solution. In equation 11, the regularization takes the form of additional costs that penalize the roughness of the q_i values. Because the model is discretized into a regular grid, for the regularization we use the Laplace filter $\mathbf{L}$ (in a regular grid in 2D, the Laplacian is approximated using the five-point-stencil finite-difference method). The μ_i are five parameters, which control the regularization weight. Increasing μ_i increases the smoothness of q_i. In the applications described below, we do not assume a prior preferential direction of the anisotropy to avoid bias in the results. This leads us to consider the same value μ for the five regularization parameters.

Construction of the tomographic system of equations

The Jacobian of the time-lapse anisotropic traveltime tomography (TLATT) $\mathbf{J}_{\text{TShift-tomography}}(\mathbf{q}) = \partial \mathbf{r}/\partial \mathbf{q}(\mathbf{q})$ can be written as a function of the trace alignment such as

$$\mathbf{J}_{\text{TShift-tomography}}(\mathbf{q}) = \underbrace{\frac{\partial \mathbf{r}}{\partial \Delta \mathbf{t}}(\mathbf{q})}_{\text{trace alignment part}} \underbrace{\frac{\partial \Delta \mathbf{t}}{\partial \mathbf{q}}}_{\text{tomographic-part}}. \tag{12}$$

The trace alignment part corresponds to $\mathbf{J}_{\text{TShift}}$. It depends on the trace alignment algorithm, which in our case is given by equation 10. The tomographic part is the traveltime perturbation due to an anisotropic velocity change. It is computed by ray tracing in the reference interval velocity model. The linearized tomography is not a limitation, and a dynamic tomography could be considered without changing the algorithm. Our rationale for using the linearized approach is because (1) perturbations are small in the overburden and (2) the dynamic approach can be unstable in certain circumstances (Jech and Pšenčík, 1989; Pratt and Chapman, 1992). The trace alignment is performed for a given window length using equations 8–10 as illustrated in Figure 2.

In the following, the model parameter $\mathbf{q}$ is discretized into a regular grid. In this representation, the traveltime perturbation due to a velocity change $\partial \Delta \mathbf{t}/\partial \mathbf{q}$ is called the tomographic matrix $\mathbf{A}$. Each row of the tomographic matrix represents a ray, and the columns of the matrix represent the cells of the model. Because the number of model parameters is five times larger than in the isotropic case, the tomography matrix is the horizontal concatenation of five matrices labeled $\mathbf{A}_k$. The coefficient a_k^{ij} at row i and column j of $\mathbf{A}_k$ stores the traveltime of the ray i in the cell j multiplied by the k-th basis function, which depends on the angle of ray i. Every row of the tomographic matrix is weighted by the Jacobian of the trace alignment (the trace alignment part of equation 11). During the nonlinear iterations of the trace alignment procedure, the trace alignment residuals and its Jacobian are updated whereas the tomographic matrix $\mathbf{A}$ remains constant. Indeed, the coefficients of the tomographic matrix (before weighting) depend on the reference model geometry and on the initial interval velocity model only. An example of the construction of the tomographic matrix is given in Appendix A.

Resolution of the nonlinear damped least-squares problem

Because the Jacobian matrix $\mathbf{J}_{\text{TShift-tomography}}(\mathbf{q})$ and the residual vector $r_{\text{TShift}}(\mathbf{q})$ depend on the velocity change $\mathbf{q}$, the least-squares minimization problem is solved iteratively (Figure 3). As described by Gubbins (2004), the velocity change is updated as $\mathbf{q}^{i+1} = \mathbf{q}^i + \delta\mathbf{q}^{i+1}$ with

$$\delta\mathbf{q}^{i+1} = (\mathbf{J}^T\mathbf{J} + \mu^2\mathbf{R}^T\mathbf{R})^{-1}(\mathbf{J}^T\mathbf{r} - \mu^2\mathbf{R}^T\mathbf{R}\mathbf{q}^i), \tag{13}$$

where $\mathbf{R}$ is the matricial representation of the regularization function (here, five Laplacian matrices $\mathbf{L}$ in a diagonal block matrix). Equation 13 shows an additional term $-\mu^2\mathbf{R}^T\mathbf{R}\mathbf{q}^i$ as compared to the linear problem, which dampens the velocity change globally. The residuals $\mathbf{r} = \mathbf{r}(\Delta\mathbf{t}^i)$ and the Jacobian matrix $\mathbf{J} = \mathbf{J}(\Delta\mathbf{t}^i)$ are updated at each increment with the obtained time shifts $\Delta\mathbf{t}^i$ computed for the last velocity change estimate $\mathbf{q}^i$ such as $\Delta\mathbf{t}^i = -\mathbf{A}\mathbf{q}^i$ (the discrete form of equation 2).

Equation 13 could be used to solve the inverse problem, but it would be very slow and difficult to compute the inverse of $\mathbf{J}^T\mathbf{J} + \mu^2\mathbf{R}^T\mathbf{R}$. Instead, we use an iterative solver proposed by Fong and Saunders (2011), which handles large and sparse matrices encountered in tomography as the rays cross a limited number of cells of the grid.

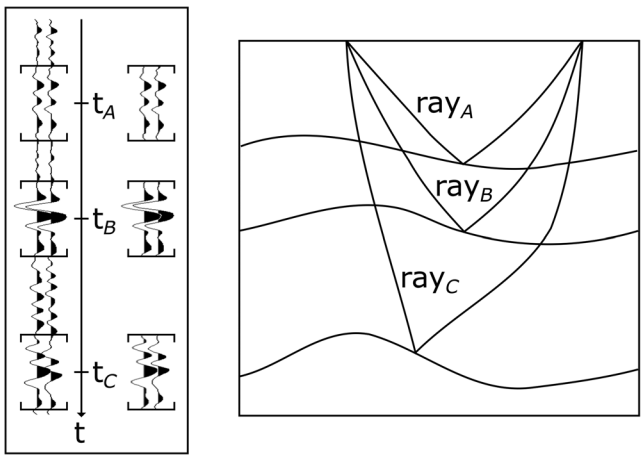

Figure 2. Trace alignment coupled with tomography for three reflectors sharing the same midpoint and offset at time t_A, t_B, and t_C. The TLATT consists of finding a velocity change $\Delta v/v$ such that the resulting time shift, given by equation 1, aligns the monitor to the baseline at the reflector time depth.

$\boldsymbol{q}^0 = \mathbf{0}$

$i = 0$

Loop until convergence criteria reached

$\boldsymbol{\Delta t}^i = -\boldsymbol{A}\boldsymbol{q}^i$

$\boldsymbol{r}^i = \boldsymbol{r}_{\mathrm{TShift}}(\boldsymbol{\Delta t}^i)$

$\boldsymbol{J}^i = \boldsymbol{J}_{\mathrm{TShift-tomography}}(\boldsymbol{\Delta t}^i)$

$\boldsymbol{\delta q}^{i+1} = \underset{\boldsymbol{x}}{\mathrm{argmin}}\left(\|\boldsymbol{J}^i\boldsymbol{x} - \boldsymbol{r}^i\|^2 + \mu^2\|\boldsymbol{R}\boldsymbol{q}^i\|^2\right)$

$\boldsymbol{q}^{i+1} = \boldsymbol{q}^i + \boldsymbol{\delta q}^{i+1}$

$i = i + 1$

End

Figure 3. Pseudocode of the coupled warping tomography algorithm.

We look for the velocity change increment $\delta\mathbf{q}^{i+1}$ solution of the equation

$$\begin{pmatrix}\mathbf{J}\\ \mu\mathbf{R}\end{pmatrix}\delta\mathbf{q}^{i+1} = \begin{pmatrix}\mathbf{r}\\ -\mu\mathbf{R}\mathbf{q}^i\end{pmatrix}, \tag{14}$$

in a least-squares sense. Our observations show that the number of nonlinear iterations varies from 3 to 10.

RESULTS

In this section, we present the results obtained on a synthetic model and a real case study. The case study is a gas field that has been in production for more than 15 years (see the reservoir seal interface in Figure 4), with a measured depletion of 150 bars. The reservoir is a carbonate platform with high porosity (28% average) sealed by low-porosity marine shales, overlaid by prodeltaic sands and fluvio/deltaic sandstones and claystones. The reservoir lies on a volcanoclastic basement. It consists of a 10 m thick gas-saturated stratigraphic series.

Interesting reflectors are picked in the base migrated stack in the depth domain (Figure 5). Because we are interested in the velocity change due to geomechanical effects at, and around, the reservoir, we picked reflectors in the over- and underburden.

The selected reflectors are used as reflection points in the ray tracing to find the reflected rays with the same common depth point (CDP) and the same offset as the prestack seismic traces. Unlike classic 1D time-lapse inversion methods that estimate a time-shift's function along the trace, our method attempts to realign the monitor to the baseline for the selected reflectors. The time shifts are not actually directly estimated. Instead, a velocity perturbation, which

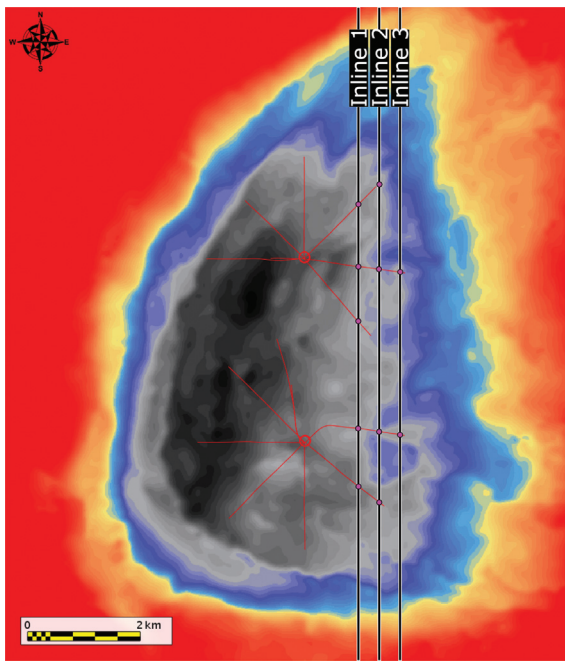

Figure 4. Basemap of the top of the carbonate platform. The three straight black lines correspond to the inline used in the analysis. The red circles represent the wellhead, and the red lines are the projected well trajectories; the wells are significantly perforated below the reservoir top.

realigns the monitor to the baseline on the selected reflectors, is retrieved and the time shifts are only an intermediate variable resulting from the trace alignment procedure.

Synthetic case

Before considering the real case study, we designed an analog synthetic data set to test the validity and applicability of the tomographic inversion. The objective of this synthetic study is to assess what TLATT can retrieve in an idealized scenario corresponding to a perfectly known baseline model and noise-free data, with similar angle coverage as in the real case. For this, we used the same geometry as the reference study. The reference velocity model used for the ray tracing is presented in Figure 6a. The velocity perturbations are described using Thomsen parameters (Thomsen, 1986) and correspond to an elliptic perturbation in a localized area of the overburden ($\varepsilon = \delta$). They can be written as

$$\frac{\Delta v}{v_0}(\theta) = \frac{\Delta v}{v_0}(0°) + \varepsilon \sin^2\theta, \tag{15}$$

where $\Delta v/v_0(0°)$ and $\varepsilon = \Delta v/v_0(90°) - \Delta v/v_0(0°)$ represent the vertical and the difference between the horizontal and the vertical time-lapse velocity change, respectively. To build the monitor model, we perturbed the baseline model with a 5% increase in the isotropic velocity in the reservoir and a 5% decrease in the vertical velocity in a relatively small area of the overburden. The vertical velocity change $\Delta v/v_0(0°)$ and the horizontal velocity change $\Delta v/v_0(90°)$ are presented in Figure 6b and 6c.

The time shifts between the base and the monitor were computed by integrating the anisotropic velocity change along rays traced on the reference velocity model, using equations 1 and 14. Because the objective of the synthetic case is to assess the ray coverage associated with the acquisition geometry, we discarded the uncertainty associated with time-shift estimation and provide the exact time shifts to the tomography. Therefore, we only study the tomography part of equation 11. We performed three experiments for three different offset ranges: the near-offset range (325–825 m), the near- to mid-offset range (325–1575 m) and the near- to far-offset range (325–2375 m) (corresponding to the real data acquisition parameters). Results are shown in Figure 7 for the five q_i parameters described in equation 7.

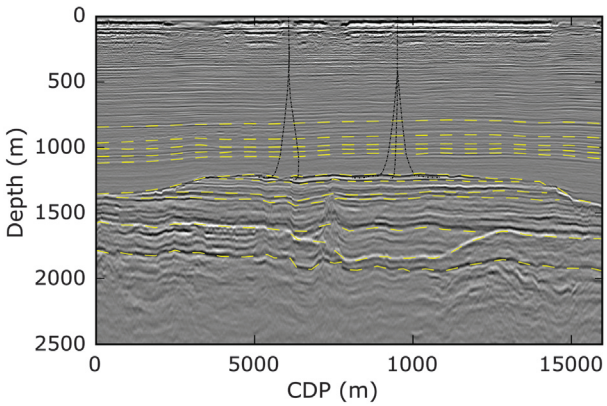

Figure 5. Depth-migrated stacked seismic of the base for the second inline (the middle one). The 12 horizons picked are drawn in the dashed yellow lines.

For the near-offset range (the first column of Figure 7), only the term q_1 (i.e., the vertical velocity change) shows a significant amplitude at the position where the isotropic anomaly was introduced in the model. It corresponds to the isotropic velocity change in the reservoir and the overburden. Indeed, for this acquisition, the rays are close to vertical rays and only q_1 is sensitive to velocity change in the vertical to subvertical direction (30° at maximum as shown in Figure 1). Some weak energy appears for q_3, but it is interpreted as a linkage between q_1 and q_3 rather than as a detection of the anisotropic anomaly. The horizontal velocity change increase is not detected in the reservoir because no horizontal rays exist.

For the larger offset range (the second and third columns of Figure 7), the main anisotropic parameters q_1, q_3, and q_5 show significant energy whereas q_2 and q_4 are almost unchanged. Indeed, q_2 and q_4 are sensitive to tilted velocity changes that were not introduced in the perturbed model. To relate the tomographic inversion results to the true velocity anomaly, a change in the parameterization is needed.

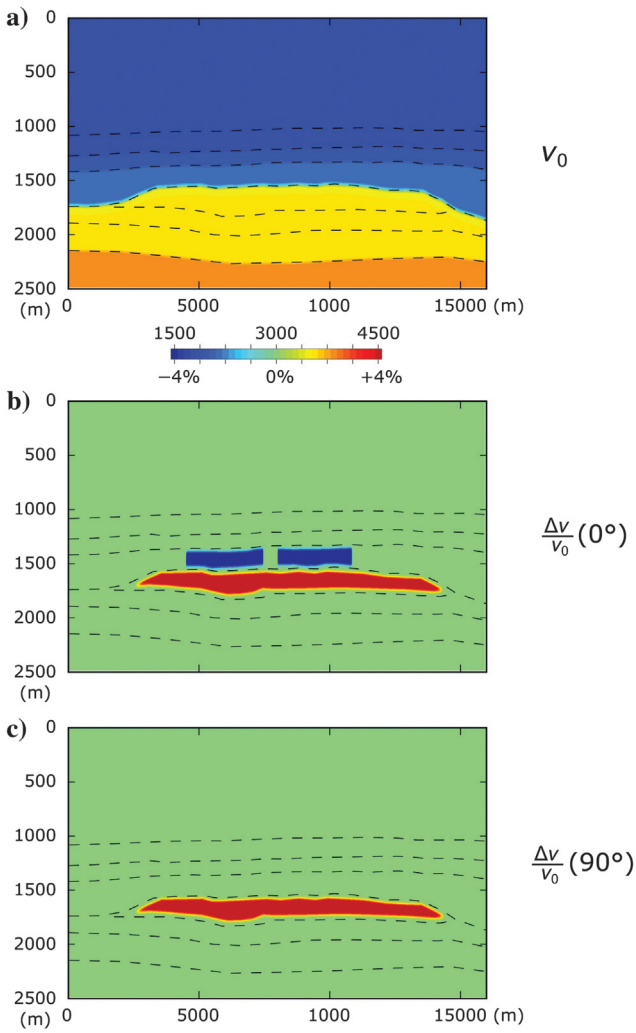

Figure 6. Synthetic dataset. (a) The reference velocity model is heterogeneous and isotropic. The longitudinal wave velocity increases gradually in the shale (the blue area), and it is chosen constant in the carbonate (the orange area). The dimensions are in meters. The ashed lines correspond to reflectors. (b) Vertical velocity change. (c) Horizontal velocity change.

We translate the three main parameters q_1, q_3, and q_5 into Thomsen parameters. The results for the near- to far-offset cases are presented in Figure 7j–7o. For the specific case of an elliptical anisotropy change, the formulas $(q_5 - q_1)$ and $2(q_3 - q_1)$ provide two different ways to estimate the elliptical anisotropy ε. The second formula works better in the case of the near- to mid-offset range because the retrieved horizontal velocity change q_5 is not reliable. Indeed, the second formula gives a higher intensity in the cap rock but a negative ε in the reservoir that is not present in the synthetic velocity perturbation. For the near- to far-offset range, both formulas provide similar results. The estimated parameters' shape and sign are correct for the isotropic and the anisotropic anomalies, but in terms of amplitude, the inverted anomalies are weaker (by a factor of almost two) compared with the true values. A possible explanation for the mismatch between the recovered amplitudes and the true ones is the influence of the regularization. Another explanation is that because the subhorizontal rays are scarce in the cap rock compared with the subvertical rays, the horizontal velocity change is less apparent than the vertical one.

The synthetic case, based on the geometry and velocity of the real case, shows that TLATT succeeds in recovering the shape, position, and sign of the anomalies. Based on this synthetic exercise, we can expect that the offset used in the real case study (325–2375 m) is large enough to obtain a reliable anisotropic time-lapse velocity change.

Application to real data

We applied the TLATT to real data from which the synthetic example is derived. This field was chosen for its anticipated strong geomechanical effect in the cap rock and the overburden. Because our method requires prestack seismic data with a large offset range, TLATT could only be performed along inlines (S/N orientation) rather than crosslines, which do not contain any mid or far offsets. Because the offshore platform obstructs the acquisition vessel, the inlines in the central part of the structure are missing in the monitor survey. The western part of the field is more complex because there is a shallower reservoir in this zone, so we decide to focus on the eastern part of the reservoir (Figure 4). We use three inlines separated by 375 m to check the consistency of the results along the crossline direction. Additional information about the repeatability of the time-lapse prestack seismic data, the interval velocity model, and the angular ray coverage, is given in Appendix B.

The tomography was performed first with an isotropic parameterization and second with an anisotropic parameterization using all of the available offsets. In both cases, 10 nonlinear iterations were needed to obtain the convergence of the system and the same regularization weights were used for each anisotropic parameter. The trace alignment was performed on a 180 ms window, which is the best compromise between the accuracy of the results (the central frequency is 30 Hz) and the stability of the solution.

Isotropic time-lapse velocity change

The tomography results for the isotropic parameterization of the three selected inlines are presented in Figure 8. We observe similar results as obtained when using 1D inversion: a velocity increase in the reservoir (due to compaction) and a decrease of velocity in the cap rock and the underburden as suggested in Sayers (2007) and Scott (2007).

The three inlines, which have been inverted independently, show an overall coherent velocity perturbation result, which is consistent with the conceptual model of a globally depleted reservoir. Moreover, the line closest to the production wells shows a stronger time-lapse effect than the lines further away from the wells. Again, this is qualitatively consistent with the expected larger pressure drop closer to production wells. The overburden velocity decrease has been observed in many time-lapse studies, but it is generally supposed to be vertical with a large extension and an arch shape. Our tomographic results show a precise location of the velocity decrease in the cap rock at the top of the produced part of the reservoir. The positive reservoir anomaly is better seen in the first (western) inline

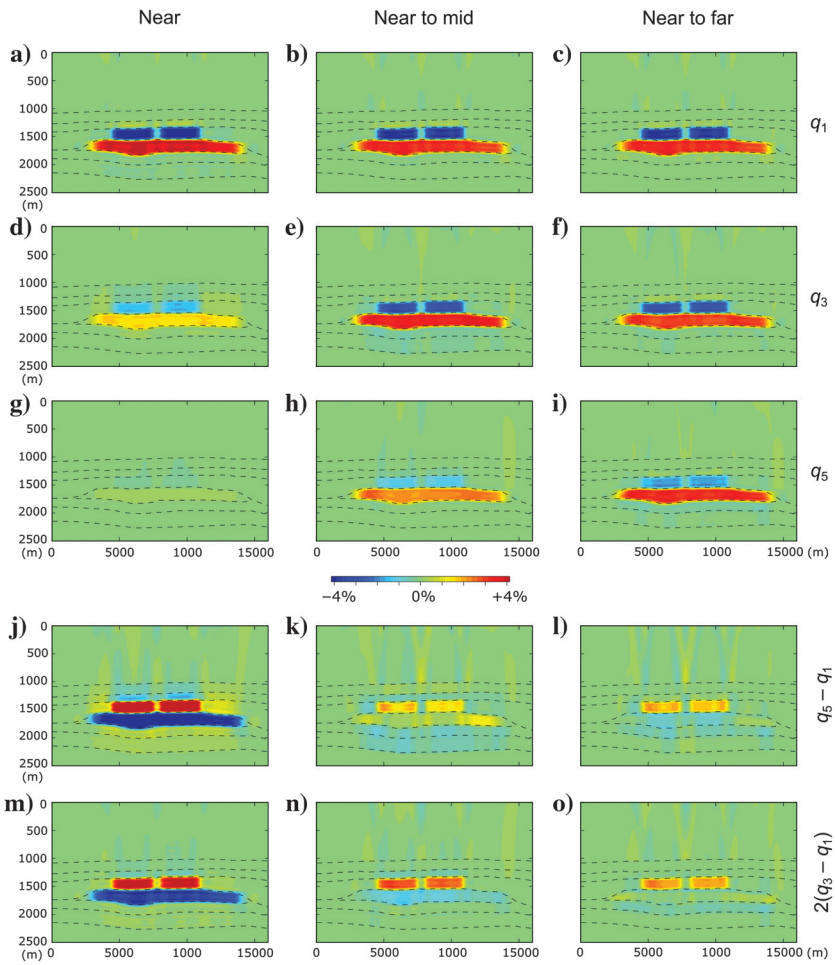

Figure 7. Anisotropic velocity changes retrieved by anisotropic reflection traveltime tomography. The columns represent the different offset acquisitions. Rows represent the anisotropic velocity change parameters q_1, q_3, and q_5 and the algebraic formula $q_5 - q_1$ (ε) and $2(q_3 - q_1)$ (δ). The parameters q_2 and q_4 are inverted but are not presented because they are equal to zero. The terms q_1 and q_5 must be compared with Figure 6b and 6c.

than in the two others. Interestingly, we can observe in the two other (eastern) inlines that the connection between the two main wells is weaker. This seems reasonable as some horizontal wells cross the first inline but do not reach the second or the third inline (Figure 4). This experiment provides good confidence on the quality of the data and therefore on the possibility of performing an anisotropic tomography.

Anisotropic time-lapse velocity change

The anisotropic velocity change is parameterized with only three parameters (q_1, q_3, and q_5), and the results are presented in Figure 9. This simplification assumes a vertical symmetry axis.

The striking observation is the weak signal recovered on q_1 whereas q_3 shows amplitudes very similar to the inverted isotropic signal (Figure 8). The second obvious result is the very strong q_5 anomaly in the cap rock, which is not present in the underburden. These observations are consistent on the three inlines. Because the acquisition is adapted to catch vertical and horizontal velocity changes, the fact that q_3 and q_5 show a high amplitude in the overburden and not q_1 can only be explained by an absence of slowdown in the vertical velocity. The observed horizontal velocity decrease in the cap rock seems to be incompatible with classic geomechanical models, which suggests the cap rock to be vertically extending and horizontally shortening.

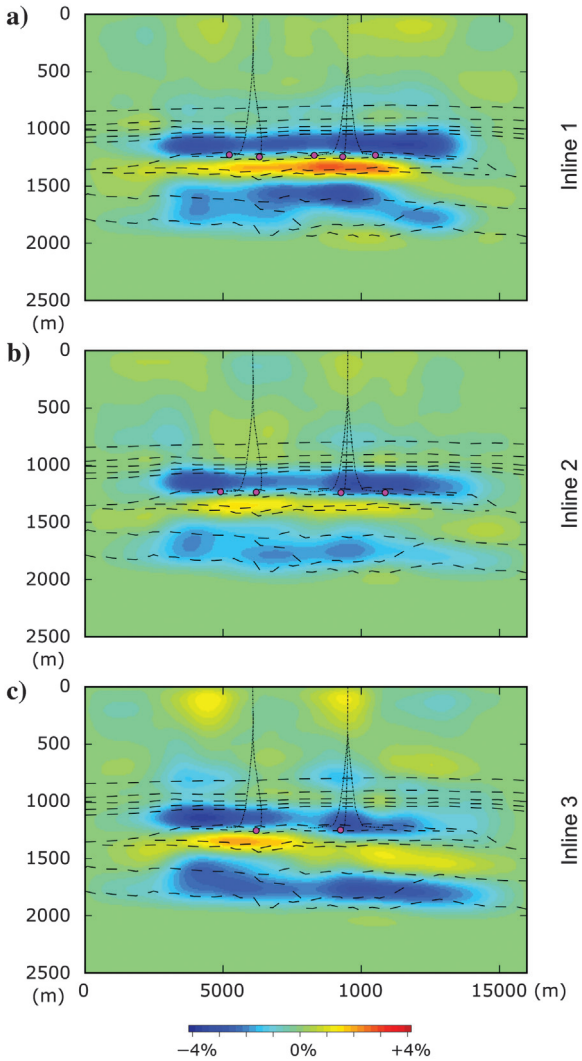

Figure 8. Isotropic velocity change retrieved by tomography for the three considered inlines. The horizons are drawn in the dashed black lines. The red anomalies correspond to a velocity increase, and they are mainly located in the reservoir. The blue anomalies correspond to a velocity slowdown and are located in the overburden and in the underburden. The projected wells are the thin dashed lines; the intersection between the wells are the image is indicated by the purple dots.

At the reservoir top, the abrupt change in velocity from approximately 2 to 3 km/s induces a critical reflection angle of approximately 40°. This corresponds to the largest offsets recorded. The estimation of the time shifts measured on a trace-by-trace basis can be hazardous if the critical angle is reached and even more if the critical angle is different in the baseline and the monitor surveys (we can roughly estimate this difference within 5° according to the estimated velocity changes). Nevertheless, during the tomography, the time shifts are not estimated individually but are the consequences of an anisotropic velocity change. Therefore, we consider that the algorithm is not too sensitive to local phase changes between the baseline and monitor data. However, the horizontal velocity decrease (q_5) measured in the cap rock (Figure 9g–9i) is mainly driven by the reservoir top time shifts observed for the largest offsets. These measurements are potentially contaminated with phase changes between the baseline and monitor surveys due to a variation of the overcritical angle, which may jeopardize the interpretation of the horizontal velocity change.

In the underburden, only the smaller angle range is available. The strong vertical velocity decrease (Figure 9a–9c) and low horizontal velocity decrease (Figure 9g–9i) could be an apparent anisotropy in the velocity change due to the lack of subhorizontal rays for retrieving the horizontal variations. Moreover, the strong reflectivity of the top of the carbonate platform makes it delicate to interpret the time shifts retrieved below the reservoir.

DISCUSSION

Because q_3 shows the strongest anomalies in the cap rock, underburden, and reservoir, the simplest interpretation is that they are due to cracks opening with an angle close to 45°. Is a single type of crack opening sufficient to explain the results observed on the isotropic and the anisotropic inversions? To answer this question, we built new synthetics with anomalies of the same amplitudes (i.e., a 5% velocity change) but affecting only q_3 and inverted them both with an isotropic (Figure 10a) and an anisotropic inversion (Figure 10b–10d). The global behavior observed on the synthetics closely matches the field-data observations in the overburden and in the reservoir, whereas disagreements remain in the underburden:

1) The isotropic inversion shows a strong velocity decrease in the cap rock, a strong increase in the velocity in the reservoir, and a slight velocity decrease in the underburden. The synthetic results match the real case isotropic inversion (Figure 7) for the reservoir and the overburden, but they disagree for the underburden.
2) The anisotropic inversion shows a strong anomaly in q_3, whereas q_1 presents a weak anomaly; q_5 shows an anomaly in the cap rock, whereas there is no anomaly in the underburden. The synthetic results match the real case anisotropic inversion

(Figure 8) for the reservoir and the overburden, but the q_1 anomaly in the underburden is not present in the synthetic inversion.

The similarity between matches synthetic and field-data results is striking, even though we cannot expect a perfect match because (1) the synthetic model is oversimplified (2) the stress regime in the reservoir and in the overburden is complex because the reservoir is inhomogeneous, and (3) measured time shifts on real data include noise not present on synthetic data. This means that the hypothesis of an existing set of fractures inducing a velocity slowdown preferentially around the 45° direction should be considered as a possible scenario.

The nonlinear elastic effect with the opening of microcracks such as those proposed by Hatchell and Bourne (2005) can explain the overburden time shifts. Previous 1D approaches used for time-lapse analysis are not able to distinguish between microstructures such as the cracks' orientation distribution, their shapes, or the nature of the contact. Hatchell and Bourne (2005) propose that a horizontal dry cracks model is a good candidate because it has a strong effect on the vertical velocity change and the opening of such cracks is predicted by a geomechanical model of reservoir depletion under normal stress conditions. However, this model is incompatible with our observations because the vertical velocity change is low. Often in ill-posed inverse problems, several explanations could probably be found. Some relate to the hypotheses made by our method, such as the ray approximation and the assumption of an initial isotropic model. However, we are confident that the consideration of small relative changes of elastic parameters justifies the ray approximation and that only very strong anisotropies in the initial model could affect the interpretation of the small observed velocity changes. It could still be interesting in future studies to compare more thoroughly and quantitatively the impact of the ray approximation by generating synthetic time-lapse data with full elastic wave simulation. Another possibility could be to apply 3D tomography, but, beyond the larger computational costs this would incur, this is not advisable on this data set because the time-lapse data do not include large offsets in the crossline direction.

The best remaining avenue to resolve the inconsistency between our observations and the classic geomechanical models is to propose plausible alternative rock-physics models. The 4D anisotropy induced by dry cracks is elliptical. Nevertheless, our real case inversion results show a 45° velocity change, which suggests that the anelliptic anisotropy in the velocity change could be due to the influence of cracks in water-saturated rock (Guéguen and Sarout, 2011). Specifically, Guéguen and Sarout (2011), model cracks as spheroidal inclusions with an aspect ratio between 10^{-2} and 10^{-3}, and they expose the velocity change-induced anisotropy for three basic crack configurations (identical cracks aligned in the same direction, identical cracks with random orientations, and cracks randomly distributed in a zone with a given axis). Therefore, vertical cracks randomly distributed in a water-saturated rock model can satisfactorily explain the results of the real case anisotropic inversion. It is to note that in a water-saturated rock, the introduction of vertical spheroidal inclusions induces a change in δ and ε compared to penny-shaped cracks (the limit case of a spheroidal inclusion with a very small aspect ratio), which induce a change in δ only. Going further to quantitatively invert for the velocity change in term of crack orientation would require the knowledge of the crack density and the crack aspect ratio, which are unknown in our case.

At first sight, the presence of vertical cracks in the overburden seems incompatible with the strain regime (vertical lengthening and horizontal shortening). In addition, the compacted area of the reservoir is approximately 100 m thick with a 12 km lateral extension, most of the strain is vertical meaning that the horizontal shortening is negligible, and the opening of vertical cracks is possible. We think that the measured anisotropy is the result of the reactivation of a preexisting fracture network. Indeed, the shale burial may create a triaxial stress regime such that the vertical stress is larger than the horizontal stress and subvertical cracks are created. The reservoir production probably reactivates preexisting weakness planes, which in our case, results in the opening of subvertical cracks filled with water.

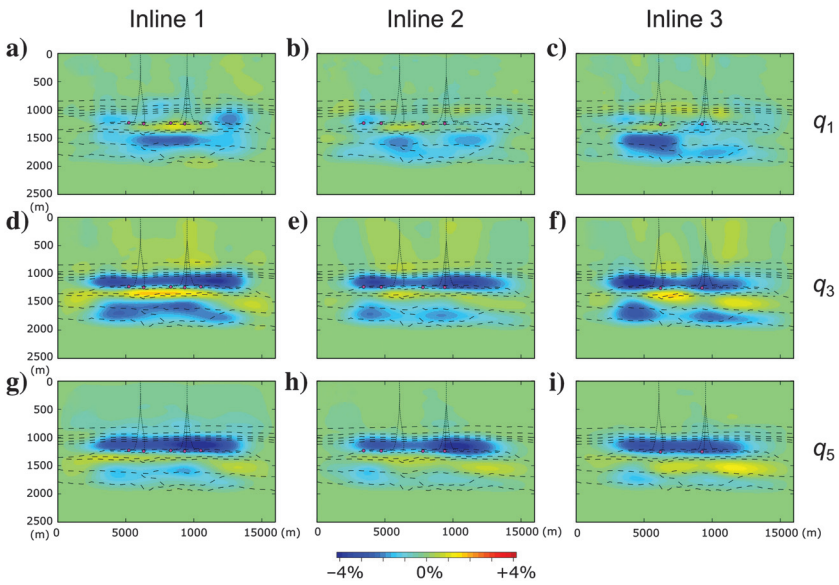

Figure 9. Anisotropic velocity change retrieved by tomography. Only the most sensitive parameters q_1, q_3, and q_5 are inverted, which is equivalent to assuming a vertical symmetry. Note that q_1, i.e., the vertical velocity change is much weaker than the isotropic velocity change presented in Figure 8.

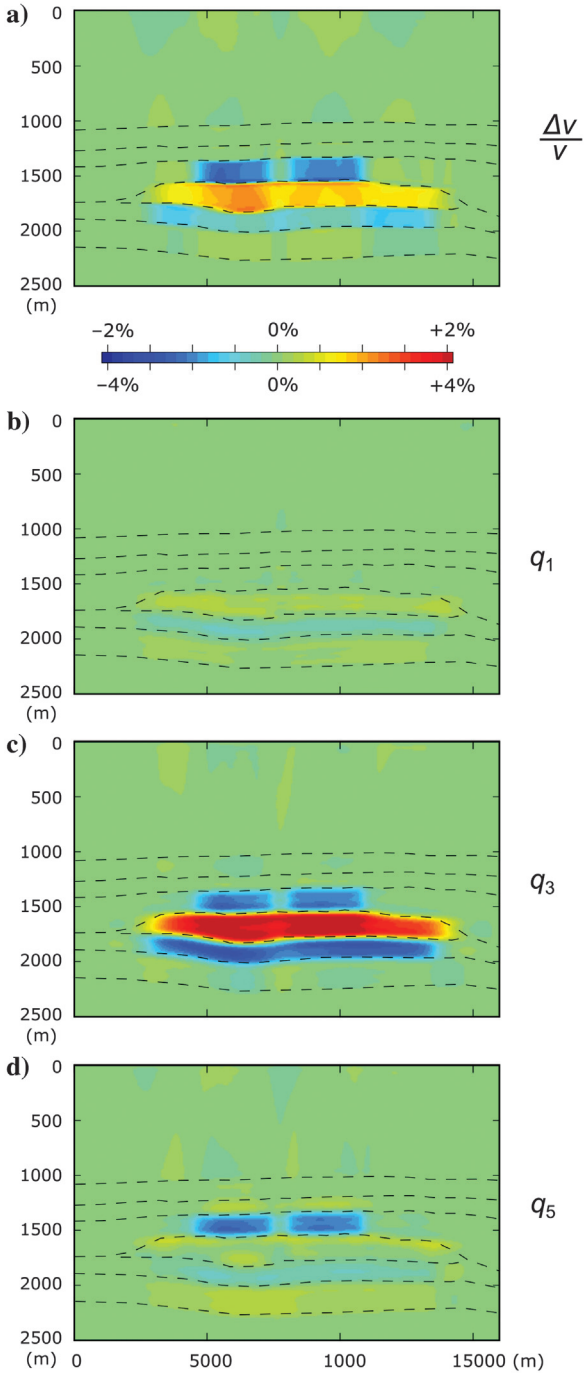

Figure 10. (a) The isotropic velocity change and (b-d) the anisotropic velocity change retrieved in the synthetic case where only a single 45° velocity change is introduced. The results are very much similar to those obtained in the real data (Figures 8 and 9). In the anisotropic case, q_1 is negligible, q_3 exhibits a strong negative anomaly in the cap rock and the overburden and a high positive anomaly in the reservoir, and q_5 shows a high negative anomaly in the cap rock.

CONCLUSION

Anisotropic time-lapse velocity changes due to reservoir compaction have been measured in a real case study. Despite the sensitivity of the tomographic method with respect to the picked horizons, the chosen trace alignment algorithm, the parameterizations, and the regularization weights, it has provided consistent results along the three studied inlines. We observe a velocity slowdown in the cap rock along the horizontal and 45° directions. In the presence of such anisotropy, the conventional 1D inversion algorithm used in time-lapse studies seems poorly adaptable to monitor the changes occurring in the cap rock because they only consider vertical velocity changes.

Classic geomechanical models show that reservoir depletion may induce an opening of horizontal cracks in the cap rock, but the anisotropic time-lapse velocity change observed in our study is incompatible with this scenario. Our interpretation is that the overburden time shifts due to the reservoir production may be due to the reactivation of a preexisting fracture network. Our tomography analysis of the overburden time shifts suggests that the time-lapse velocity change is likely a function of an intrinsic property of the rock (weakness planes). The proposed monitoring method provides new insight into elaborating geomechanical models and stress-dependent rock-physics models calibrated with time-lapse seismic data.

ACKNOWLEDGMENTS

We would like to thank Total and the ANRT for funding the Ph.D. of N. Mastio. We also thank Total for the permission to publish the results. We would like to acknowledge A. Giraud, J. Fortin, and Y. Leroy for discussions during the realization of this work. Finally, we thank V. Kazei and three anonymous reviewers who helped to improve this paper.

DATA AND MATERIALS AVAILABILITY

We can provide the synthetic dataset created for testing the method.

APPENDIX A

TOMOGRAPHIC MATRIX EXAMPLES

Here, we present a simple example on how to construct tomographic matrix **A**. For the sake of simplicity, we present the construction procedure for only one ray, which results in a single-row tomographic matrix. The space is discretized in 4×4 regular grid as illustrated in Figure A-1.

The ray trajectory is discretized by points sampled at a regular time interval dt. The ray traveltime restricted to each cell of the grid is then approximated as the number of ray points within each cell times the sampling interval dt, and it can be written in the matrix

$$\begin{pmatrix} 9 & 4 & 0 & 15 \\ 0 & 12 & 10 & 3 \\ 0 & 13 & 12 & 0 \\ 0 & 9 & 0 & 0 \end{pmatrix} dt. \qquad \text{(A-1)}$$

The error in one cell is bounded by $4dt$ if the ray twice crosses the same cell. To increase the tomography matrix accuracy, the regular grid can be coarser and the time interval can be shorter.

Because a ray is represented by one row of the tomographic matrix such, we rewrite matrix A-1 in the tomographic matrix as

$$\boldsymbol{A}_{\text{iso}} = \begin{pmatrix} & & & & \vdots & & & \\ 9 & 4 & 0 & 15 & 0 & 12 & 10 & \cdots \\ & & & & \vdots & & & \end{pmatrix} dt. \quad \text{(A-2)}$$

In the presence of anisotropy, the velocity change $\Delta v/v_0$ is a function of the polar angle θ parameterized by five basis functions $f_k(\theta)$ as

$$\frac{\Delta v}{v_0}(\theta) = \sum_{k=1}^{5} q_k f_k(\theta). \quad \text{(A-3)}$$

The anisotropic tomographic matrix is the horizontal concatenation of five matrices, which have the same dimension as the isotropic matrix but where all coefficients are weighted by $f_k(\theta)$. To illustrate this, we write the k-part of one row of the anisotropic tomographic matrix $\boldsymbol{A}^k_{\text{ani}}$ using the same rectangular representation as in equation A-1

$$\boldsymbol{A}^k_{\text{ani}} = \begin{pmatrix} 9f_k(\theta_1) & 4f_k(\theta_2) & 0 & 15f_k(\theta_4) \\ 0 & 12f_k(\theta_6) & 10f_k(\theta_7) & 3f_k(\theta_8) \\ 0 & 12f_k(\theta_{10}^{\text{down}}) + f_k(\theta_{10}^{\text{up}}) & 12f_k(\theta_{11}) & 0 \\ 0 & 4f_k(\theta_{14}^{\text{down}}) + 5f_k(\theta_{14}^{\text{up}}) & 0 & 0 \end{pmatrix} dt. \quad \text{(A-4)}$$

The term θ_j is the polar angle of the ray at the cell j. For presentation purpose, we decompose the ray in two parts (one corresponding to the downgoing wavefield and one corresponding to the reflected upgoing wavefield). In practice, this angle is known at each ray discretization point, so the value $f_k(\theta)dt$ is accumulated during the ray tracing.

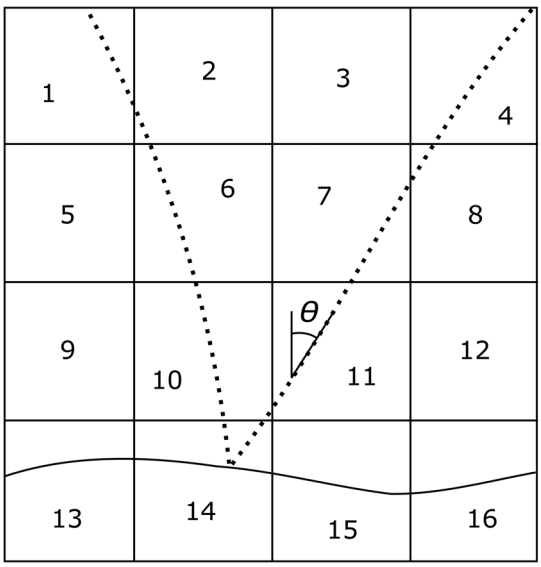

Figure A-1. A simplistic example on the construction of the tomographic matrix. The model is divided into 16 cells. The reflected ray is sampled at regular time steps which are represented by the dots. The traveltime spent by the ray at each cell is estimated by counting the number of dots in the cell and multiplying it by the time step.

APPENDIX B

CASE STUDY SEISMIC ACQUISITION AND PREPROCESSING

The base and monitor vessel air guns shoot at a regular interval of 25 m, which is translated in the data with CDPs every 25 m. Nevertheless, the air guns, hydrophone arrays, and number of streamers are different between the acquisitions of the base and the monitor. To address the source difference, the two acquisitions have been processed to comply with 4D standards in terms of equalization and spectrum. The distance between hydrophone arrays of the base and the monitor is 33.33 and 25 m, respectively, which means that it is not possible to find a trace that corresponds to the same couple of source and receiver in both acquisitions. The traces were sorted into 43 offset classes (0 to 300, 300 to 350, ..., 2350 to 2400 m). The first offset class has a larger interval and was excluded from the analysis because the traces' offset differences between the base and the monitor are often very large in this class, and it induces a moveout larger than the time-lapse time shifts. For the 42 other classes, the offset differences are reduced considerably but the induced normal moveout still needs to be corrected. Indeed, we study small overburden time shifts, and this area is close enough to the surface to be affected by the offset difference. To solve this issue, we interpolated all the traces of these 42 offset classes to the middle offsets (325, 375, ..., 2375 m) by applying a time shift along the trace. This time shift δt is estimated using the differentiation of the reflection traveltime with respect to the offset:

$$\delta t = \frac{x \delta x}{t v_{\text{RMS}}^2}, \quad \text{(B-1)}$$

where t is the two-way vertical traveltime (i.e., the trace depth in time), v_{RMS} is the root-mean-square velocity, x is the offset of the trace, and δx is the difference between the offset of the trace and the middle offset. This interpolation is valid for the considered data set because most of the seismic energy is reflected. After interpolation, the baseline and monitor traces share the same CDP and offset.

The interval velocity model (Figure B-1) used for ray tracing was created from the v_{RMS} model using smoothing and the Dix equation (an inverse approach procedure). Some far-offset rays are presented to assess the ray angle coverage. The traveltime of the reflected rays is also used as a quality check (Figure B-2).

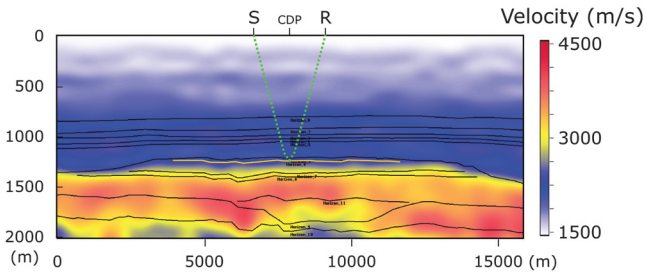

Figure B-1. The internal velocity model used for ray tracing. A far offset ray is plotted in green.

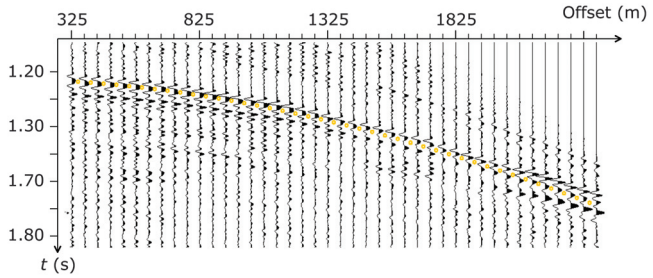

Figure B-2. Prestack seismic traces of one CDP of the base. The ray-computed traveltimes for one reflection surface are indicated with the yellow circle.

REFERENCES

Aki, K., and P. Richards, 2002, Quantitative seismology, 2nd ed.: University Science Books.

Alkhalifah, T., 1997, Seismic data processing in vertically inhomogeneous TI media: Geophysics, **62**, 662–675, doi: 10.1190/1.1444175.

Alkhalifah, T., and R. Plessix, 2014, A recipe for practical full-waveform inversion in anisotropic media: An analytical parameter resolution study: Geophysics, **79**, no. 3, R91–R101, doi: 10.1190/geo2013-0366.1.

Backus, G., 1970, A geometrical picture of anisotropic elastic tensors: Reviews of Geophysics, **8**, 633–671, doi: 10.1029/RG008i003p00633.

Barkved, O. I., and T. Kristiansen, 2005, Seismic time-lapse effects and stress changes: Examples from a compacting reservoir: The Leading Edge, **24**, 1244–1248, doi: 10.1190/1.2149636.

Červený, V., 2001, Seismic ray theory: Cambridge University Press.

Chapman, C. H., and R. G. Pratt, 1992, Traveltime tomography in anisotropic media — 1: Theory: Geophysical Journal International, **109**, 1–19, doi: 10.1111/j.1365-246X.1992.tb00075.x.

De Gennaro, S., A. Onaisi, A. Grandi, L. Ben-Brahim, and V. Neillo, 2008, 4D reservoir geomechanics: A case study from the HP/HT reservoirs of the Elgin and Franklin fields: First Break, **26**, 53–59, doi: 10.3997/1365-2397.2008019.

Dybvik, O. P., L. Gemmer, U. Theune, and S. Østmo, 2009, Establishing a geomechanical workflow for time-lapse modelling of an HPHT field: 71st Annual International Conference and Exhibition, EAGE, Extended Abstracts, P343.

Edgar, J. A., and N. Mastio, 2017, Time-lapse velocity change tomography: 79th Annual International Conference and Exhibition, EAGE, Extended Abstracts, A114.

Every, A. G., and W. Sachse, 1992, Sensitivity of inversion algorithms for recovering elastic constants of anisotropic solids from longitudinal wavespeed data: Ultrasonics, **30**, 43–48, doi: 10.1016/0041-624X(92)90031-G.

Fong, D. C.-L., and M. Saunders, 2011, LSMR: An iterative algorithm for sparse least-squares problems: SIAM Journal on Scientific Computing, **33**, 2950–2971, doi: 10.1137/10079687X.

Fuck, R. F., A. Bakulin, and I. Tsvankin, 2009, Theory of traveltime shifts around compacting reservoirs: 3D solutions for heterogeneous anisotropic media: Geophysics, **74**, no. 1, D25–D36, doi: 10.1190/1.3033215.

Gubbins, D., 2004, Time series analysis and inverse theory for geophysicists: Cambridge University Press, 131–132.

Guéguen, Y., and J. Sarout, 2011, Characteristics of anisotropy and dispersion in cracked medium: Tectonophysics, **503**, 165–172, doi: 10.1016/j.tecto.2010.09.021.

Guilbot, J., and B. Smith, 2002, 4-D constrained depth conversion for reservoir compaction estimation: Application to Ekofisk field: The Leading Edge, **21**, 302–308, doi: 10.1190/1.1463782.

Hale, D., 2013, Dynamic warping of seismic images: Geophysics, **78**, no. 2, S105–S115, doi: 10.1190/geo2012-0327.1.

Hatchell, P., and S. Bourne, 2005, Rocks under strain: Strain-induced time-lapse time shifts are observed for depleting reservoirs: The Leading Edge, **24**, 1222–1225, doi: 10.1190/1.2149624.

Hatchell, P., R. Kawar, and A. Savitski, 2005, Integrating 4D seismic, geomechanics and reservoir simulation in the Valhall oil field: 67th Annual International Conference and Exhibition, EAGE, Extended Abstracts, C012.

Hearmon, R., 1953, 'Third-order' elastic coefficients: Acta Crystallographica, **6**, 331–340, doi: 10.1107/S0365110X53000909.

Herwanger, J. V., and S. A. Horne, 2009, Linking reservoir geomechanics and time-lapse seismics: Predicting anisotropic velocity changes and seismic attributes: Geophysics, **74**, no. 4, W13–W33, doi: 10.1190/1.3122407.

Jech, J., and I. Pšenčík, 1989, First-order perturbation method for anisotropic media: Geophysical Journal International, **99**, 369–376, doi: 10.1111/j.1365-246X.1989.tb01694.x.

Kazei, K., and T. Alkhalifah, 2018a, Scattering radiation pattern Atlas: What anisotropic elastic properties can body waves resolve? Journal of Geophysical Research, Solid Earth, **124**, 2781–2811, doi: 10.1029/2018JB016687.

Kazei, V., and T. Alkhalifah, 2018b, Waveform inversion for orthorhombic anisotropy with P waves: Feasibility and resolution: Geophysical Journal International, **213**, 963–982, doi: 10.1093/gji/ggy034.

Le Bégat, S., and V. Farra, 1997, P-wave traveltime and polarization tomography of VSP data: Geophysical Journal International, **131**, 100–114, doi: 10.1111/j.1365-246X.1997.tb00597.x.

Love, A., 1944, A treatise on the mathematical theory of elasticity, 4th ed.: Dover Publications.

MacBeth, C., 2002, Multi-component VSP analysis for applied seismic anisotropy: Pergamon, Seismic Exploration Series, **26**.

Mikesell, T. D., A. E. Malcolm, D. Yang, and M. M. Haney, 2015, A comparison of methods to estimate seismic phase delays: Numerical examples for coda wave interferometry: Geophysical Journal International, **202**, 347–360, doi: 10.1093/gji/ggv138.

Nolet, G., 1987, Seismic tomography: With applications in global seismology and exploration geophysics: Springer, Seismology and Exploration Geophysics, **5**, 1–23.

Nowack, R. L., and I. Pšenčík, 1991, Perturbation from isotropic to anisotropic heterogeneous media in the ray approximation: Geophysical Journal International, **106**, 1–10, doi: 10.1111/j.1365-246X.1991.tb04597.x.

Oh, J., and T. Alkhalifah, 2016, The scattering potential of partial derivative wavefields in 3D elastic orthorhombic media: An inversion prospective: Geophysical Journal International, **206**, 1740–1760, doi: 10.1093/gji/ggw238.

Podgornova, O., S. Leaney, and L. Liang, 2018, Resolution of VTI anisotropy with elastic full-waveform inversion: Theory and basic numerical examples: Geophysical Journal International, **214**, 200–218, doi: 10.1093/gji/ggy116.

Pratt, R. G., and C. H. Chapman, 1992, Traveltime tomography in anisotropic media—II Application: Geophysical Journal International, **109**, 20–37.

Prieux, V., R. Brossier, Y. Gholami, S. Operto, J. Virieux, O. I. Barkved, and J. H. Kommedal, 2011, On the footprint of anisotropy on isotropic full waveform inversion: The Valhall case study: Geophysical Journal International, **187**, 1495–1515, doi: 10.1111/j.1365-246X.2011.05209.x.

Prioul, R., A. Bakulin, and V. Bakulin, 2004, Nonlinear rock physics model for estimation of 3D subsurface stress in anisotropic formations: Theory and laboratory verification: Geophysics, **69**, 415–425, doi: 10.1190/1.1707061.

Rickett, J., L. Duranti, T. Hudson, B. Regel, and N. Hodgson, 2007, 4D time strain and the seismic signature of geomechanical compaction at Genesis: The Leading Edge, **26**, 644–647, doi: 10.1190/1.2737103.

Rodriguez-Herrera, A., N. Koutsabeloulis, A. Onaisi, J. Fiore, and F. Selva, 2015, Stress-induced signatures in 4D seismic data: Evidence of overburden stress arching: 85th Annual International Meeting, SEG, Expanded Abstracts, 5368–5372.

Røste, T., O. P. Dybvik, and O. K. Søreide, 2015, Overburden 4D time shifts induced by reservoir compaction at Snorre field: The Leading Edge, **34**, 1366–1374, doi: 10.1190/tle34111366.1.

Røste, T., A. Stovas, and M. Landrø, 2006, Estimation of layer thickness and velocity changes using 4D prestack seismic data: Geophysics, **71**, no. 6, S219–S234, doi: 10.1190/1.2335657.

Sayers, C. M., 2007, Asymmetry in the time-lapse seismic response to injection and depletion: Geophysical Prospecting, **55**, 699–705, doi: 10.1111/j.1365-2478.2007.00636.x.

Scott, T. E., Jr., 2007, The effects of stress paths on acoustic velocities and 4D seismic imaging: The Leading Edge, **26**, 602–608, doi: 10.1190/1.2737101.

Thomsen, L., 1986, Weak elastic anisotropy: Geophysics, **51**, 1954–1966, doi: 10.1190/1.1442051.

Williamson, P., A. Cherrett, and P. Sexton, 2007, A new approach to warping for quantitative time-lapse characterization: 69th Annual International Conference and Exhibition, EAGE, Extended Abstracts, P064.